

Powder Metallurgy Route for the Synthesis of Multiprincipal Element Alloys Sputtering Targets

Elena Colombini, Magdalena Lassinantti Gualtieri,* Cecilia Mortalò,*
Silvia Maria Deambrosis, Francesco Montagner, Valentina Zin, Enrico Miorin,
Giorgio Valsecchi, Monica Fabrizio, and Paolo Veronesi

Sputter deposition of multiprincipal element alloys (MPEAs) is a relatively new field of research with high functional potential. The multicomponent design space is immense and practically unexplored. An important obstacle for academic research of such sputtered films is the availability of single-alloy targets and technical difficulties in using cosputtering of multiple metal targets or powder targets. This article focuses on the development of a simple powder metallurgy route, including cold uniaxial pressing of powder mixtures followed by pressureless sintering, for the preparation of targets made of two common base alloys forming simple solid solutions, i.e., FeNiCrCo and FeNiCrMn. In addition, targets of the former one containing 10 at% Al are also prepared. The sintered pellets are composed of randomly oriented crystallites with face-centered cubic structures and an optimum chemical homogeneity. Oxide inclusions and residual porosity, inherent to consolidation and sintering of metal precursors, are observed and possible solutions to overcome these challenging problems are discussed. Nevertheless, encouraging results from preliminary deposition tests of FeNiCrCoAl_{0.4} using both direct current magnetron sputtering (DCMS) and high-power impulse magnetron sputtering (HiPIMS) are presented.

coined by Yeh and co-workers who attributed the stabilization of simple solid solution phases, often observed in these systems, to high configurational entropy.^[2] Restrictions were set on both number of principal elements (≥ 5) and their concentrations (5–35 at%).^[2] In a recent review, Miracle and Senkov suggested to use the broader terms multiprincipal element alloys (MPEAs), complex concentration alloys (CCAs), and baseless alloys (BAS) in order to better conceptualize the immense design space offered by nonconventional alloys without putting limits on composition and microstructure.^[4]

The 3d transition metal family of MPEAs is by far the most studied one and it can be compared to stainless steels and superalloys.^[4] This family contains at least four of the elements Al, Co, Cr, Cu, Fe, Mn, Ni, Ti, and V.^[4] Common 4-element branches of this popular alloy family are FeNiCrCo and FeNiCrMn. Being comparable to commercial structural materials, much work has been focused on mechanical properties and their relations to composition and microstructure. In particular, the distinct roles played by Al, Sn, and Nb have been evidenced.^[4] Another important area of study is the environmental resistance of structural materials in terms of, e.g., corrosion and wear resistance.^[4]


1. Introduction

With the advent of high-entropy alloys (HEAs) in the early 2000s,^[1,2] the research activities in the branch of physical metallurgy gained new momentum as witnessed by the huge amount of papers produced on these materials.^[3–5] The specific term was

commercial structural materials, much work has been focused on mechanical properties and their relations to composition and microstructure. In particular, the distinct roles played by Al, Sn, and Nb have been evidenced.^[4] Another important area of study is the environmental resistance of structural materials in terms of, e.g., corrosion and wear resistance.^[4]

E. Colombini, M. Lassinantti Gualtieri, P. Veronesi
Department of Engineering “Enzo Ferrari”
University of Modena and Reggio Emilia
Via Pietro Vivarelli 10/1, 41125 Modena, Italy
E-mail: magdalena.gualtieri@unimore.it

M. Lassinantti Gualtieri
Interdepartmental Research Centre for Applied Research and Services in
the Advanced Mechanics and Motor Sector
University of Modena and Reggio Emilia
Via Pietro Vivarelli 2, 41125 Modena, Italy

 The ORCID identification number(s) for the author(s) of this article can be found under <https://doi.org/10.1002/adem.202101518>.

© 2022 The Authors. Advanced Engineering Materials published by Wiley-VCH GmbH. This is an open access article under the terms of the Creative Commons Attribution License, which permits use, distribution and reproduction in any medium, provided the original work is properly cited.

DOI: 10.1002/adem.202101518

C. Mortalò, S. M. Deambrosis, F. Montagner, V. Zin, E. Miorin, M. Fabrizio
National Research Council of Italy - CNR
Institute of Condensed Matter Chemistry and Technologies for Energy –
ICMATE
Corso Stati Uniti, 4, 35127 Padova, Italy
E-mail: cecilia.mortalo@cnr.it

G. Valsecchi
R&D department
TAV VACUUM FURNACES SPA
Via dell'Industria 11, 24043 Caravaggio (BG), Italy

M. Fabrizio
CNR Engineering ICT and Technologies for Energy and Transportation
Department
National Research Council of Italy
P.le A. Moro 7, 00185 Roma, Italy

Bulk MPEAs are generally prepared by conventional ingot (e.g., arc melting, induction melting) or powder metallurgy (PM) routes. The latter methods generally involve prealloyed powders (either mechanically alloyed or atomized) which are consolidated by spark plasma sintering (SPS), hot isostatic pressing (HIP), or cold pressing followed by vacuum sintering.^[6–8] More rarely, consolidation and in situ alloying of elemental powders has been utilized.^[9–17] The latter PM approach offers the important advantage of being less complicated and expensive as the production of prealloyed powders is avoided. Numerous 3d transition metal MPEAs with simple microstructures (face-centered cubic [fcc], body-centered cubic [bcc]) have been synthesized using various techniques for consolidation and in situ alloying: pressing and subsequent sintering either in Ar^[9] or under vacuum,^[10–12] SPS,^[13–15] pressing, and subsequent sintering with the aid of microwaves.^[16,17]

An important drawback of PM routes is oxide contamination, as recently pointed out by Fourmont and co-workers.^[15] These authors synthesized dual-phase AlCoCrFeNi MPEAs (fcc + bcc) by SPS of mechanically activated powders.^[15] Although a good chemical homogeneity of the phases was obtained, contaminating nanooxides (i.e., Al₂O₃ and Cr₂O₃) were found. Careful chemical analyses after the various processing steps evidenced that most of the oxygen contamination came from the starting commercial powders. This result highlights a crucial factor that may compromise the purity of alloys synthesized by the PM route.

MPEAs can also be synthesized as films/coatings by physical vapor deposition (PVD) techniques.^[18,19] In particular, magnetron sputtering (MS) deposition is gaining interest as the film properties can be tailored by varying the target composition and process parameters. In addition, nitride, oxide, and carbide-containing MPEAs can be fabricated by using reactive gas during the process.^[18,20] Films and coatings of MPEAs have been shown to possess high hardness and elastic modulus, good wear and corrosion resistance in addition to interesting electrical and magnetic properties.^[21]

Sputtering deposition of MPEAs is generally achieved by 1) cosputtering of multiple metal targets or mosaic targets;^[22–27] 2) sputtering from a single MPEA target generally obtained either by casting^[28–41] or by PM;^[42–45] and 3) sputtering of metal targets which are fabricated by cold pressing powder mixtures.^[46,47]

Generally, cosputtering of MPEAs has been used when investigating the effect of an additive on the properties of the film.^[24] For example, Bachani et al. deposited VNbMoTaWAl films while varying the Al-content by cosputtering of an equimolar VNbMoTaW target together with a pure Al-target.^[24] The concomitant use of several single element targets for the deposition of multicomponent films with controlled properties becomes technically challenging, especially with the prospect of depositing homogeneous coatings on substrates with complex shapes. Hence, most work on MPEA sputtering on such substrates has employed prealloyed targets. However, regarding powder targets (mixed powders), a major advantage is the ease of preparation. Nevertheless, their use is not straightforward for magnetron sputtering of MPEAs containing elements that are ferromagnetic in their pure state.^[48] Indeed, targets of ferromagnetic materials influence the magnetic field of the sputtering system and suitable approaches are therefore required to ensure stable

deposition conditions (e.g., instrumental adjustments, modification of target geometry, heating above the Curie point of the target).^[48] For paramagnetic prealloyed MPEAs (e.g., FeNiCrMn^[49] and FeNiCrCo^[50]) containing ferromagnetic elements, alloy targets are advantageous. For sputtering of ferromagnetic MPEAs such as equiatomic FeCrNiCoAl,^[50] cosputtering of paramagnetic FeNiCrCo alloy target and Al single target may be a valid option.

Hence, the need to prepare prealloyed magnetron sputtering sources through relatively simple and easily accessible methodologies becomes evident. To this aim, this work deals with the development of a simple powder metallurgy route, including cold pressing of mixed elemental powders followed by pressureless sintering, for the preparation of MPEAs pellets and sputtering targets. The chosen methodology is promising for in-house production of MPEAs targets without the need of advanced metallurgical equipment (e.g., SPS, HIP). Encouraging results from preliminary deposition tests using both direct current magnetron sputtering (DCMS) and high-power impulse magnetron sputtering (HiPIMS), the latter combining MS technology with high power pulse technology,^[51] will be presented.

2. Experimental Section

2.1. Sample Preparation

The starting metal powders used in this work were: iron (Aldrich, 97%), nickel (Alfa Aesar, 99.8%), manganese (Aldrich, 99%), cobalt (Alfa Aesar, 99.8%), chromium (Alfa Aesar, 99%), and aluminum (Alfa Aesar, 99.5%). Powder mixtures with the compositions FeNiCrCo, FeNiCrMn, and FeNiCrCoAl_x ($x = 0.4$) were prepared as follows: metal precursors were mixed for 1 h in a planetary ball mill (PM100, Retsch GmbH, Haan, Gemania) operating at 250 rpm in argon atmosphere. The grinding jar (stainless steel, 250 mL) was charged with 50 g of powder and 500 g of grinding balls (stainless steel, \varnothing 5–15 mm). Grinding was stopped every 15 min for 10 min to avoid excessive heating. Contamination from the milling media was excluded as no weight change was recorded neither for the balls nor for the jar.

For preliminary sintering tests, cylindrical pellets with a diameter of 20 mm and thickness of ≈ 7 mm were prepared by direct uniaxial pressing (30 s at 140 MPa followed by 99 s at 640 MPa) using a semiautomatic press (Nannetti, Mod. Mignon-S). The same equipment was used to prepare FeNiCrCoAl_{0.4} sputtering targets with a diameter of 50 mm.

The sintering treatments were carried out using the TAV 718 H3-TPH 30-345-TP all metal cold wall oven (heating power 190 kW, maximum working temperature 1450 °C with uniformity of 5 °C in the loading volume, final vacuum 10⁻⁴ Pa, operating vacuum 10⁻³ Pa). Green pellets were placed on alumina supports and heated (3.3 °C min⁻¹) up to 400 °C in high vacuum conditions and subsequently under Ar atmosphere (5 kPa) up to the selected temperature (T_{max}).

The green pellets were sintered at two different maximum temperatures (T_{max}), i.e., 1200 and 1300 °C with an isotherm of 4 h at T_{max} , while the green target for sputtering was sintered at 1300 °C with an isotherm of 6 h at T_{max} . Natural cooling to room temperature was conducted under Ar.

Table 1. Main sputtering parameters used when depositing FeNiCrCoAl_{0.4} thin films with DCMS and HiPIMS.

	V [V]	Average I [mA]	I peak [A]	HiPIMS f [Hz]	Pulse time [μs]	Bias voltage [V]	Bias f [Hz]	Bias pulse time [μs]
DCMS	478	210	/	/	/	35	/	/
HiPIMS	760	133	12	250	100	35	250	200

For the sputtering experiments, the leveled and polished target was mounted on a MAK (5 cm diameter) source (MeiVac Incorporation, San Jose, California, USA) and fixed to a spherical 600 mm diameter vacuum chamber. The depositions were conducted in DCMS mode using a True Plasma DC generator series 3000 power supply (TRUMPF-Hüttinger) or in HiPIMS mode using a HiPSTER 6 power supply (6 kW maximum power, Ionautics AB, Sweden). The employed bias unit was a HiPSTER 1 (Ionautics AB, Sweden) for all deposited specimens.

Si wafers (100) with a thickness of 0.6 mm were chosen as test substrates and the sample holder was not heated during the deposition process. Total working pressure was set at 0.5 Pa (Ar 99.999% purity), the selected average power was 100 W, target-substrate distance was fixed at 70 mm, while deposition duration was 120 min. The main sputtering parameters are summarized in Table 1.

2.2. Characterization Methods

The particle size distributions of powders were analyzed by laser particle size analyzer (Mastersizer 2000, Malvern), while the specific surface area (SSA) was measured by gas adsorption using a Gemini 2360 from Micromeritics.

The volumes of green and sintered samples that were used to calculate apparent densities (ρ_{app}) were determined from dimensional measurements and water displacement data, respectively. The real density (ρ_r) of green pellets was calculated from the nominal composition of the precursor mixture and the real density of each component as given by the manufacturer. Instead, the real density of sintered pellets was determined from X-ray powder diffraction (XRPD) data and Rietveld refinements (see below). Relative densities (RD) were calculated using ρ_r as reference (i.e., ρ_{app}/ρ_r).

The mean grain size was determined by optical microscopy analyses (LEICA EZ4D) of polished and etched samples. In order to evidence the grain boundaries, etching of FeNiCrMn samples was achieved with Nital solution (95 vol% ethanol+5 vol% concentrated nitric acid) for 2 min, whereas a treatment in aqua regia for (30–75 s) was conducted for Co-containing specimen. Following etching, the samples were rinsed in distilled water and consequently washed in ethanol under ultrasonic action for 5 min. Samples were subsequently dried in hot air.

XRPD data were collected for powders and sintered pellets, as well as for sputtered films using a symmetric parallel beam configuration. The instrument used was a multipurpose X'Pert PRO (PANalytical, Almelo, The Netherlands) diffractometer equipped with a Cu K α source (40 kV and 40 mA). The diverging Cu-K radiation emitted from the X-ray tube was converted to a quasiparallel beam using an X-ray mirror. A beam mask of 20 mm was used to limit the beam width. The diffracted beam path included a parallel plate collimator, a detector slit,

soller slits (0.04 rad), a flat graphite monochromator, and a gas proportional counter.

The sintered samples were mounted with the surface of the disc-shaped samples perpendicular to the diffraction vector. Before the measurement, the surface was grinded to remove at least 1.5–2 mm of the outer surface. Data were collected in the 2θ range 5°–130° using a step size of 0.02° and 8 s step⁻¹. The symmetrical parallel beam configuration allows to accurately determine the positions of the Bragg reflections. In fact, the calculated cell parameter of a LaB₆ standard (660a from the National Institute of Standard and Technology, NIST) used for calibration purposes was 0.415694 ± 0.000002 nm, which perfectly corresponds to that certified by NIST, i.e., 0.415692 ± 0.000001 .^[52]

Rietveld refinements were performed using freely available software (General Structure Analysis System, GSAS^[53]) in conjunction with its graphical interface EXPGUI.^[54] A multiterm Simpson's rule integration of the pseudo-Voigt function was used to model the peak profiles, whereas the background was fitted with a shifted Chebyshev function with six to nine terms. Scale factors and unit cell parameters were refined. The $K\alpha_1/K\alpha_2$ ratio, polarization, and peak asymmetry were calibrated using data collected from the standard (LaB₆, 660a from NIST). A fcc ($Fd\bar{3}m$) structure model was used for the alloy, assuming a random solid solution with site occupancy reflecting the nominal composition.

Line profile parameters of each Bragg reflection of the alloy structure as well as for the standard (660a, NIST) were extracted by profile fitting. The peaks were modeled with a pseudo-Voigt function using the software ProFit (Philips Electronics N.V., version 1.0c). The peak position, intensity, full width at half maximum (FWHM), and the shape parameter (also called mixing parameter, η) of the pseudo-Voigt function were refined in addition to the background. The peak positions were used to calculate the lattice constants.

The thickness of the sputtered coatings was determined by using a ball crater microabrasion method (Calotest Anton Paar). Data were subsequently used to evaluate deposition rates.

An environmental SEM (ESEM Quanta-200, FEI Company) equipped with an INCA-350 energy-dispersive X-ray spectroscopy (EDS) detector (Oxford Instruments) was used to analyze the powders. Morphological and compositional characterizations of sintered compacts and sputtered films were performed by field emission SEM (FESEM; Nova NanoSEM 450, FEI Company, equipped with X-EDS Quantax-200, Bruker). Both surface and cross section of samples were analyzed. On the other hand, sputtered films were investigated by a similar FESEM microscope from Zeiss (Sigma instrument equipped with a X-Max EDS system from Oxford Instruments). Mean size of pores and oxide inclusions were determined using the image analysis software ImageJ.^[55]

3. Results and Discussions

3.1. Powders

The median diameters of the powders measured by laser diffraction (Figure S1, Supporting Information) were Fe 18.9 μm ; Cr 27.5 μm ; Ni 9.9 μm ; Co 8.4 μm ; Mn 25.2 μm ; and Al 10.1 μm . This size order is in agreement with SEM images (Figure S2, Supporting Information). Rapid ball-milling, aimed at accurately mixing the constituent powders, did not cause important phase changes such as oxidation or alloying. In fact, XRPD patterns collected from the mixed powders exhibited only the peaks belonging to the starting metal precursors (see Figure S3, Supporting Information). Although no oxides were detected in the XRPD patterns, it is assumed that some contamination of oxygen is present. In fact, as recently demonstrated by Fourmont et al., commercial powders of Al, Co, Cr, Fe, and Ni contain surface passivation layers that result in a total oxygen content of 0.6 wt% in an equimolar mixture.^[15] It is interesting to observe that grinding resulted in cold welding of the particles in the Co-containing system, even more pronounced when Al was added. Indeed, the particle size distributions measured by laser diffraction increased to higher values after ball-milling (see Figure S4a,b, Supporting Information). The opposite trend was observed for the Mn-containing powder mixture, where grinding resulted in a particle size reduction (see Figure S4c, Supporting Information) due to the Mn comminution and lack of cold welding caused by aluminum. The observed changes in particle size were mirrored in the SSA results. Indeed, a significantly lower SSA was detected for the FeNiCrCo and FeNiCrAl_{0.4} systems after mixing, while the opposite behavior was observed for FeNiCrMn (see Table S1, Supporting Information).

3.2. Pellets

3.2.1. Density, Porosity, and Grain Size

The sintering of the green pellets was expected to result in both densification and homogenization of the solid phase through diffusion of the constituent atoms. Both processes are considered

positive for the development of sputtering targets. Indeed, high apparent density (ρ_{app}) and the formation of a paramagnetic MPEA are desirable characteristics for efficient and stable depositions by magnetron sputtering. **Table 2** shows the apparent densities (ρ_{app}) of the pellets before and after sintering at different temperatures. The RD of the sintered compacts were calculated assuming a real density (ρ_r) corresponding to a pure fcc alloy and were therefore underestimated due to the presence of low-density oxides, as will be discussed later (Section 3.2.2). Nevertheless, the data allow to confirm the expected trends. Table 2 also includes the mean grain size determined from polished and etched samples.

RD of the green pellets of about 0.7 are reasonable considering the applied maximum pressure (640 MPa) (see Table 2). Moreover, no lubricants were added to limit interparticle friction.^[56] Consequently, some residual porosity is observed in the sintered pellets (see Table 2). The thermal treatment at 1200 °C determined an increase in RD of the FeNiCrCo and FeNiCrMn alloys (Table 2), whereas no variation of RD was observed for FeNiCrCoAl_{0.4}. Despite the presence of a low-melting point element (i.e., Al), the conditions for effective transient liquid phase sintering were apparently not favorable in the latter system. Possible contributing factors are 1) the presence of oxide envelopes on the Al grains that hinder penetration of the liquid metal into the surrounding pores; 2) poor wetting of the particles by the liquid metal,^[57,58] and 3) fast diffusion of Al into the solid phase which leads to swelling and the formation of secondary porosity.^[58]

Higher RD were achieved by increasing the sintering temperature from 1200 °C to 1300 °C for the FeNiCrCo and FeNiCrCoAl_{0.4} alloys (Table 2). Instead, no further densification was obtained for FeNiCrMn, which reached a RD value higher than 0.9 already at 1200 °C.

Generally speaking, pores in sputtering targets should be limited as they may negatively affect the evolution of collisional cascades and heat conduction during sputtering. Nevertheless, these effects are highly dependent on the porous structure of the target and the system as a whole, including materials characteristics and the sputtering setup.^[59,60] Hence, it is difficult to determine a priori sputtering stability and coating quality based only on RD.

Table 2. Apparent densities (ρ_{app}) and RD of green and sintered pellets. The estimated total pore volume (V_p) in % is also reported together with the mean grain size.

	FeNiCrCo		FeNiCrCoAl _{0.4}		FeNiCrMn	
ρ_{app} green [g cm ⁻³]	5.96 ± 0.03		5.62 ± 0.07		5.50 ± 0.07	
RD green	0.724 ± 0.004		0.71 ± 0.01		0.70 ± 0.01	
V_p green [%]	27.6		29		30	
T_{max} [°C]	1200	1300	1200	1300	1200	1300
ρ_{app} sintered [g cm ⁻³]	6.43 ± 0.04	6.91 ± 0.04	5.50 ± 0.07	6.06 ± 0.07	7.02 ± 0.06	7.02 ± 0.05
RD sintered ^{a)}	0.781 ± 0.005	0.840 ± 0.005	0.72 ± 0.01	0.79 ± 0.01	0.908 ± 0.007	0.908 ± 0.006
V_p sintered [%] ^{a)}	22.9	16.0	28	21	9.2	9.2
Mean grain size [μm]	4 ± 2	5 ± 3	2.1 ± 0.7	2.8 ± 0.7	12 ± 6	500–3000

^{a)}The value of ρ_r was obtained from XRPD data and Rietveld refinements (fcc structure model assuming random solid solution with site occupancy reflecting the nominal composition, see Section 3.2.2). The reported RD is thus underestimated as the presence of low-density oxides is not considered. The ρ_r of the overall solid phase (fcc alloy+oxides) is surely lower. As a consequence, V_p is overestimated.

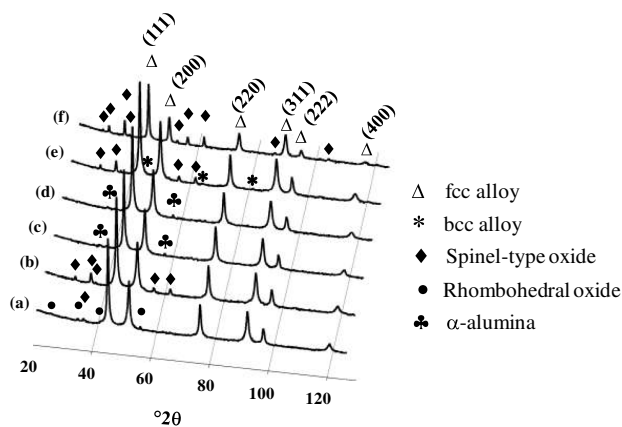


Figure 1. X-ray diffraction (XRD) patterns collected from sintered samples (square-root intensity scale): a) FeNiCrCo at 1200 °C; b) FeNiCrCo at 1300 °C; c) FeNiCrCoAl_{0.4} at 1200 °C; d) FeNiCrCoAl_{0.4} at 1300 °C; e) FeNiCrMn at 1200 °C; and f) FeNiCrMn at 1300 °C. Main peaks are indexed as fcc structure. Minor oxide phases are present; spinel-type oxide (peaks identified by rhombs); rhombohedral oxide (possible Cr₂O₃, PDF number 01-084-0313 identified by black circles), and α-alumina in the system containing Al (identified by clovers). The FeNiCrMn alloy annealed at 1200 °C also contains minor amount of bcc structure, indicated by stars.

3.2.2. XRPD

Figure 1 shows the XRPD patterns collected from the various MPEAs sintered at two different temperatures. All samples show simple diffraction patterns, with a single-phase fcc structure (peaks indexed in Figure 1) with the exception of the FeNiCrMn alloy synthesized at 1200 °C, which also contains a trace amount of a bcc structure (star symbol in Figure 1e). Zooms of the angular regions containing the main peaks of this phase are shown in Figure S5a,b, Supporting Information. The absence of fcc-based ordered structures such as L1₂ and L1₀ also indicates a random solid solution, which is stabilized by high mixing configurational entropy. Hence, alloying was achieved above possible order–disorder transition temperature (ODT) (i.e., temperature above which the system is disordered and below which the system shows partial ordering).^[61]

Minor amounts of oxides were also detected. More precisely, spinel-type oxides were identified in FeNiCrMn (Cr_{1.5}Mn_{1.5}O₄)^[62] and FeNiCrCo compositions sintered at 1300 °C (Fe–Cr spinel oxide^[63]). For the FeNiCrCo alloy sintered at 1200 °C, in addition to the spinel phase a rhombohedral oxide (Cr₂O₃)^[64] was also recognized (see zoom of selected angular regions in Figure S5c, Supporting Information). Instead, the patterns collected from the FeNiCrCoAl_{0.4} alloy contain peaks having positions and relative intensities that perfectly match α-Al₂O₃, the only thermodynamically stable polymorph of alumina. The origin of oxide contaminants within the synthesized alloys is mainly attributed to the passivating oxide layers present in the commercial powders.^[15] In addition, the powder mixing procedure applied in this work (i.e., rapid ball-milling) probably deteriorated these layers and thus liberated new metallic surface that oxidized when exposed to ambient conditions during later processing steps (i.e., die loading, uniaxial pressing). It is interesting to observe that pure oxides of Ni, Co, and Fe were

not detected in the sintered pellets (Figure 1) even though the starting powders of these metals are also oxidized.^[15] Fourmont et al. explained this result by a reorganization of the oxide phases at high temperature according to the Ellingham diagram that predicts the reduction of oxides of Ni, Co, and Fe through redox reactions with Al and Cr.^[15]

Regarding the alloy phase formation evidenced in Figure 1, data are in line with what is reported in the literature. Miracle and Senkov recently reviewed the phase composition of multi-component alloys following various synthesis methods and post-synthesis processing.^[4] The author concluded that almost all fcc solid solution alloys belong to the 3d transition metal MPEA, the typical compositions of which are CoCr_xFeNi (0.5 < x < 1.15) and Al_xCoCrFeNi (x < 0.3).^[4] Simple fcc powder patterns have been reported for Al_xCoCrFeNi MPEAs with x < 0.5 (i.e., <11.1 at%).^[65] Bracq et al. studied the stability of the fcc solid solution in the Co–Cr–Fe–Mn–Ni system both experimentally from annealed ingots and from quinary phase diagrams calculated by the Calphad approach.^[66] The equiatomic FeNiCrMn alloy was mainly composed of a fcc phase with a minor amount of bcc phase, a result which was in line with calculated composition.^[66] A multiphase composition of this system was also reported by Wu et al. for arc-melted ingots that were homogenized for 24 h at 1100 °C prior to analysis.^[67] Dahlborg et al.^[68] have recently shown that the equimolar base alloy FeNiCrCo, which is generally considered a true solid solution, is actually not a single phase but consists of at least two fcc structures with slightly different lattice constant only clearly quantifiable by high-energy XRD.^[68]

The diffractions peaks of the fcc alloys appear broad (Figure 1), a feature that is best emphasized in **Figure 2** which shows the integral breadth as a function of 2θ for the alloy profiles as well as from the profiles of a standard reference material representing the instrumental broadening. The identification of the physical origin of line broadening in these materials may be rather complex. Locally varying compositions can result in a different lattice spacing that could cause a microstrain-like broadening.^[69,70] In addition, MPEAs may be composed of distinct structures having the same crystal symmetry but slightly different lattice constants,^[11,67] resulting in an apparent broadening or asymmetry of peaks.

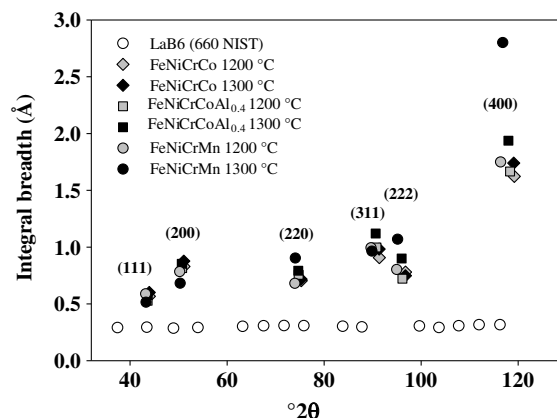


Figure 2. The integral breadth versus 2θ for the profiles of sintered HEAs as well as for the LaB₆ NIST 660a standard. The Miller indices (hkl) are displayed.

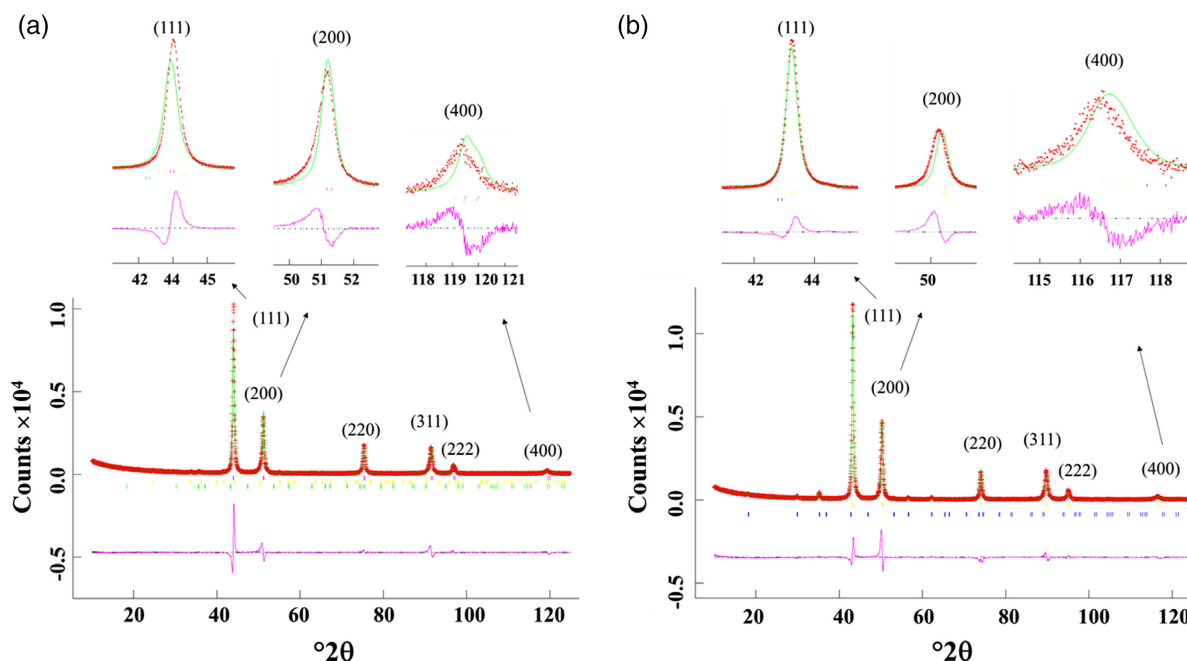


Figure 3. The Rietveld refinement output of the FeNiCrCo (a) and the FeNiCrMn (b) alloy annealed at 1200 °C. The observed, calculated, and difference curve are depicted. The vertical bars mark the positions of Bragg reflection: a) from the top: fcc phase, Cr₂O₃^[64]; Fe–Cr spinel oxide^[63]; b) from the top: fcc phase; Mn–Cr spinel oxide.^[62] The bcc phase observed in FeNiCrMn (b) was omitted due to low peak intensities. The insets in each figure show selected 2θ ranges better elucidating the abnormal shifts observed for the reflections corresponding to the planes (200) and (400).

Considering these facts, line broadening analyses using classical integral breadth methods become challenging as they are based on peak fitting of single reflections.^[71] The intrinsically low resolution reached by the symmetric parallel beam configuration used in this work^[72] does not allow to exclude the presence of such a multiphase system in the studied samples.

Rietveld refinements were performed in an attempt to fit the diffraction patterns with a fcc (*Fd-3m*) structure model assuming a random solid solution with site occupancy reflecting the nominal composition of the alloy. As an example, **Figure 3** shows the fit of FeNiCrCo (a) and FeNiCrMn (b) annealed at 1200 °C. A

rather good fit of relative intensities is observed, indicating randomly oriented crystallites. However, the model fails to properly fit the positions of reflections with Miller indices (200) and (400) that appear shifted at lower 2θ angles (see insets in Figure 3). This effect is also observed for the reflection indexed as (311) but to a lower extent. This apparent distortion of the unit cell was also reflected in differences in calculated lattice constants.

Figure 4 shows the lattice constants calculated separately from the refined position of each reflection in the various alloys. Each horizontal line corresponds to the average value for a given data set (indicated in the right side of the figure).

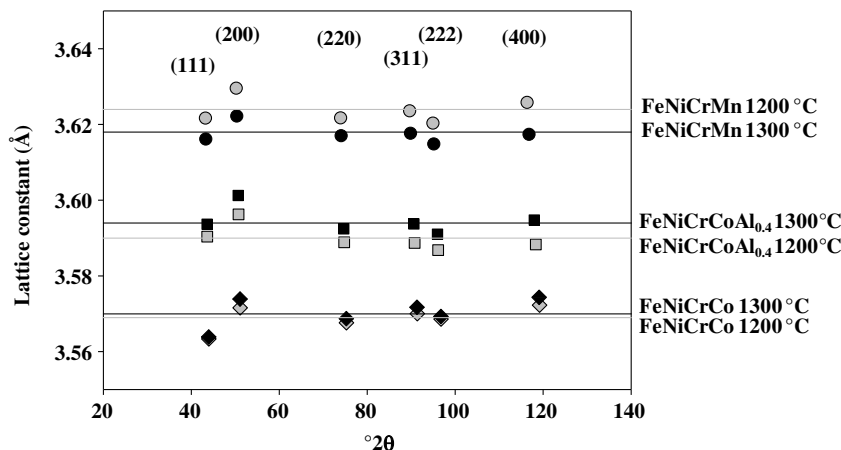


Figure 4. Lattice constants derived separately from each Bragg reflection with Miller indices (*hkl*). Data from alloys sintered at 1200 °C (gray symbols) and 1300 °C (black symbols) are shown. Errors are within symbols.

Table 3. Mean value of the lattice constants calculated from the refined position of each reflection in the diffractograms collected from the various alloys.

T [°C]	FeNiCrCo		FeNiCrCoAl _{0.4}		FeNiCrMn	
	1200	1300	1200	1300	1200	1300
a [Å]	3.569 ± 0.003	3.570 ± 0.004	3.590 ± 0.003	3.594 ± 0.003	3.624 ± 0.003	3.618 ± 0.002

To facilitate comparisons, the mean lattice constants are also reported in **Table 3**.

First of all, the data in Figure 4 and Table 3 evidence the following decreasing trend in the lattice constant: FeNiCrCo < FeNiCrCoAl_{0.4} < FeNiCrMn. The smaller lattice constant observed in the FeNiCrCo alloy is congruent with the empirical correlation observed between this parameter and the atomic radius of constituting elements.^[73] The addition of Al in the FeNiCrCo system is expected to expand the fcc unit cell due to the larger atomic radius of this element (1.43 Å) with respect to Fe (1.26 Å), Ni (1.24 Å), Cr (1.28 Å), and Co (1.25 Å).^[73] Likewise, the substitution of Co with Mn should lead to an increased unit cell due to the larger atomic radius of the latter element (1.27 Å). The larger lattice parameter observed in FeNiCrMn with respect to FeNiCrCoAl_{0.4} is not expected considering only a strict correlation between atomic radii and lattice constant as the mean atomic radius for FeNiCrMn is smaller than for FeNiCrCoAl_{0.4} (1.26 and 1.28 Å, respectively). A detailed explanation for this observation should not only take into account the actual composition of the fcc phase (differing from the nominal one due to presence of Al₂O₃ in FeNiCrCoAl_{0.4} systems and mixed CrMn oxides in FeNiCrMn) and the distribution of atoms within the structure, but also the interactions between atoms during alloying.^[73] In fact, local charge transfer and distortion may alter the effective atomic radii in the alloy with respect to the pure elements.^[73] For example, Wang and co-workers found a more important increase in lattice parameter of Ni fcc with Re as additive with respect to Al, even though the latter element has a larger atomic radius with respect to the former, i.e., 1.43 Å with respect to 1.37 Å.^[73] The same considerations may be evoked when discussing the differences in lattice constants between samples sintered at various temperatures as observed in the FeNiCrMn and FeNiCrCoAl_{0.4} alloys (see Figure 4).

Assuming a perfect and relaxed structure, the calculated lattice constant should be the same regardless of which Bragg reflection is considered. This was not observed in the MPEAs investigated here (see Figure 4). Dahlberg et al. investigated the structure of multicomponent FeNiCrCo and FeNiCrCoPd alloys synthesized by arc-melting before and after various heat treatments and found that lattice constants derived from the reflections indexed as (200) and (400) were abnormally high for the as-cast alloys.^[68] A definite distortion of the cubic fcc structure was given as a possible explanation for these observations, later confirmed for Pd-doped NiCoFeCr alloys by Zhang and co-workers.^[74] Instead, Liu and co-workers obtained a near-perfect fit between experimental and calculated patterns when performing Rietveld analyses of the equiatomic FeNiCrCo alloy prepared by sintering of atomized alloy powders.^[75] A good fit of the fcc structure was also reported by Owen et al.^[76] for a gas atomized CrMnFeCoNi equiatomic powder sintered at 1200 °C for 2 h followed by water quenching. Hence, the anomalous shifts at the lower 2θ angle of

the reflections 200 and 400 that were reported in earlier works and observed here appear to be related to the synthesis conditions and therefore to the microstructure. Interestingly, the same anomalous peak shifts are observed in patterns collected from the so-called expanded austenite (or S-phase) which is formed following the incorporation of nitrogen or carbon in austenitic stainless steels.^[77] Among the numerous models that have been proposed to explain these observations, the presence of stacking faults and/or elastic anisotropy seems to be the most accepted ones.^[77,78] Indeed, fcc MPEAs show an elastic anisotropy similar to that of simple fcc metals and alloys with the ratio of the elastic stiffness in the <111> direction over that in the <100> direction being 1.98 which is similar to pure nickel (2.17).^[79] Further studies regarding the cause of the lattice distortions in MPEAs observed in this work and in those by others are needed.

In conclusion, the XRPD analyses did not allow to exclude the possibility of a heterogeneous distribution of the elements on a microscopic scale. Nevertheless, in view of using the sintered alloys as sputtering targets, minor concentration fluctuations of the constituting elements in the target are not important as the composition of sputtered layers is determined by the average stoichiometry of the sputtering target.^[80,81]

3.2.3. Microstructural evaluations by SEM-EDS

Figure 5 shows back-scattered electron (BSE) SEM images of the three different systems sintered at 1200 and 1300 °C. High-resolution images of each system sintered at 1300 °C are shown in **Figure 6**. The spatial resolution allows obtaining a general picture of pores and oxide inclusions on a micrometer scale. As already discussed in the previous section, the oxides originate from the passivation layers present in the powders that reorganize at high temperature through redox reactions in which metallic Al, Cr, and Mn act as reducing agents of Fe–Ni and Co oxides.

Both residual porosity and oxide inclusion are present in FeNiCrCo (Figure 5a,d) and FeNiCrCoAl_{0.4} alloys (Figure 5b,e), whereas the latter dominate in the FeNiCrMn alloys (Figure 5c,f). The oxide inclusions in the FeNiCrCo and FeNiCrCoAl_{0.4} systems are more clearly visible in Figure 6a and b, respectively. The figures also evidence the presence of oxides in the pores. EDS analyses confirm the XRPD results reported in Section 3.2.2, showing Cr-rich and Cr–Mn-rich oxides in the FeNiCrCo and FeNiCrMn, respectively, and Al oxide in the FeNiCrCoAl_{0.4} system. As a consequence, the bulks of the sintered alloys were slightly depleted of the oxidized metals with respect to the nominal composition (not shown here). The presence of mixed Cr–Mn oxides with different stoichiometry was even better highlighted at higher magnifications (see BSE-SEM images shown in Figure S6, Supporting Information). Indeed, the presence of phase contrast (supported by EDS analyses) within the oxide inclusions was evidenced.

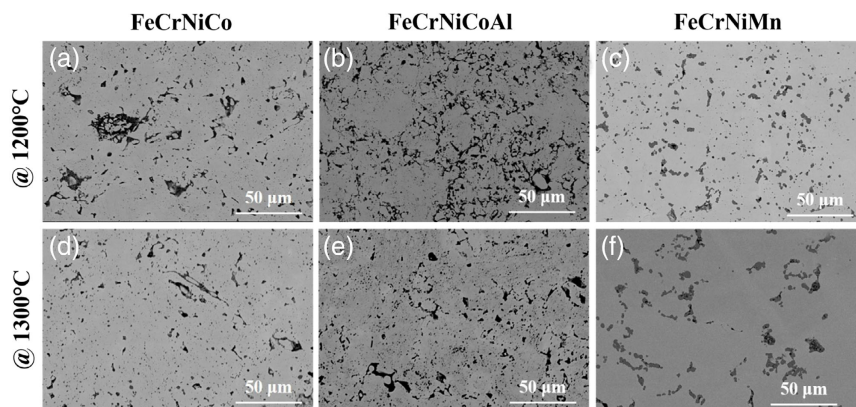


Figure 5. BSE-SEM micrographs of the cross section of a,d) FeNiCrCo, b,e) FeNiCrCoAl_{0.4}, and c,f) FeNiCrMn sintered at 1200 °C and 1300 °C.

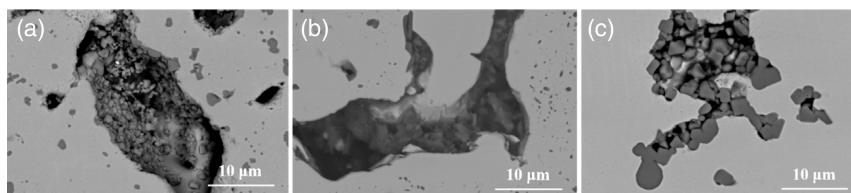


Figure 6. BSE-SEM micrographs of the cross section of a) FeNiCrCo, b) FeNiCrCoAl_{0.4}, and c) FeNiCrMn sintered at 1300 °C.

Qualitative evaluations of pores and oxide inclusions observable in Figure 5 support the data reported in Table 2, i.e., an increase in RD with sintering temperature for FeNiCrCo and FeNiCrCoAl_{0.4}. According to image analyses, the mean pore size decreases from ≈ 13 to $6 \mu\text{m}^2$ when the sintering temperature was increased from 1200 to 1300 °C in the FeNiCrCo system. The corresponding values for sintered FeNiCrCoAl_{0.4} pellets were ≈ 6 and $4 \mu\text{m}^2$. In the FeNiCrMn alloy (d,f), a coarsening of the inclusions with sintering temperature is observed. In fact, image analyses showed an increase in mean size from ≈ 5 to $15 \mu\text{m}^2$.

To further investigate the phase composition of the alloy matrices, high-resolution BSE micrographs were recorded and representative images of samples sintered at 1300 °C are shown in Figure 7. Although the close atomic numbers of the constituent elements made this type of analysis rather challenging, the images show some compositional variations represented by different contrasts. The most pronounced contrast differences were observed in the FeNiCrMn alloy containing lighter areas that, according to EDS analyses, were enriched in Ni and Mn compared to darker ones. Elemental segregation in HEAs has

often been observed despite being a single-phase solution crystallographic structure.^[82] To conclude, SEM observations are in agreement with XRPD analyses, suggesting the presence of areas with different metal compositions in sintered specimen. However, considering their application as targets for PVD depositions, this possible heterogeneous distribution of the elements on a microscopic scale should not negatively affect the final composition of sputtered layers that is determined by the average stoichiometry of the sputtering target.^[80,81]

3.3. FeNiCrCoAl_{0.4} Sputtering Targets and Deposited Coatings

MPEA coatings were successfully deposited from the produced FeNiCrCoAl_{0.4} target in both DCMS and HiPIMS mode, showing that the preparation method is effective for the realization of an efficient sputtering source.

Microstructural investigations of the sintered target confirmed the results obtained from smaller pellets, namely, the formation of randomly oriented fcc crystallites and minor inclusions of α -alumina. Figure S7, Supporting Information, shows

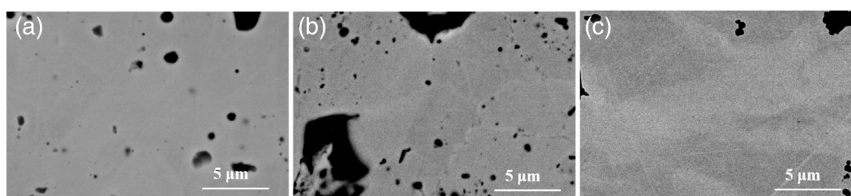


Figure 7. BSE-SEM micrographs of the cross section of FeCrNiCo, FeCrNiCoAl_{0.4}, and FeCrNiMn samples sintered at 1300 °C.

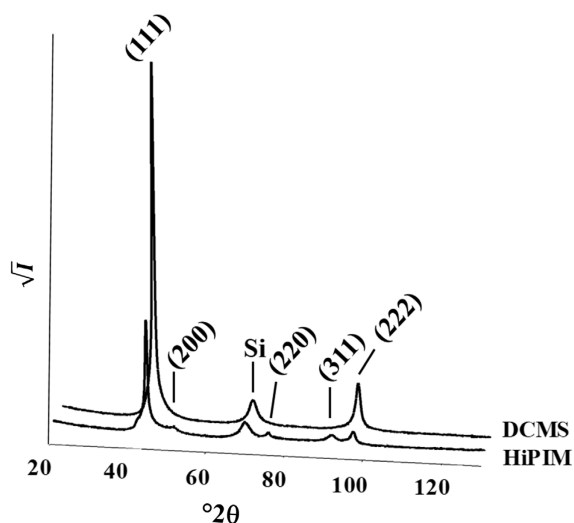


Figure 8. XRD patterns collected from sputtered films, showing a fcc structure (indexed). The crystallites are preferentially oriented with the [111] direction perpendicular to the substrate surface. The 400 peak of the silicon substrate is also present.

photographs of the sintered target (a) and the magnetron in operation (HiPIMS mode) during the deposition process (b). The target surface was positioned parallel to the Si substrates, which rotated during sputtering to promote the homogeneity of the growing coatings. The process was stable in both DC and pulsed mode. **Figure 8** displays the XRPD patterns collected from sputtered films, showing the desired fcc crystallites (indexed). The 400 reflection of the Si wafer is also indicated. The relative intensities of the 111 and 222 reflections are higher with respect to a randomly oriented pattern, indicating a preferred orientation of the [111] direction perpendicular to the substrate surface. A small shoulder is also observed on the low-angle side of the (111) peak ($d \approx 2.2 \text{ \AA}$) (see **Figure 8**).

A conclusive identification of this diffraction signal on the basis of the data collected hitherto is not possible. Nevertheless, the formation of some intermetallic phase or a secondary random solid solution with slightly different unit cell with respect to the main fcc phase can be hypothesized.

Figure 9 shows SEM micrographs of the top surfaces and cross sections of the MPEA films. The film sputtered in DCMS mode appeared less smooth than the one prepared using HiPIMS technology (see **Figure 9a,b**). This phenomenon is due to the presence of a higher fraction of ionized particles when using HiPIMS technology (with the same average power).^[83] The ultrasmooth surface is attributed to the enhancement of atom mobility mediated by energetic bombardment.^[83] Looking at the cross sections, both coatings appear dense, compact, and homogeneous. The deposition rate is lower with HiPIMS than with DCMS (13.3 nm min^{-1} with respect to 21.7 nm min^{-1}). Consequently, a thicker film was obtained with the DCMS technology as can be observed in **Figures 9c,d**. The thickness measured by Calotest was 2.6 and $1.6 \text{ }\mu\text{m}$ for films deposited by DCMS and HiPIMS, respectively. The lower deposition rate obtained with HiPIMS with respect to DCMS is due to

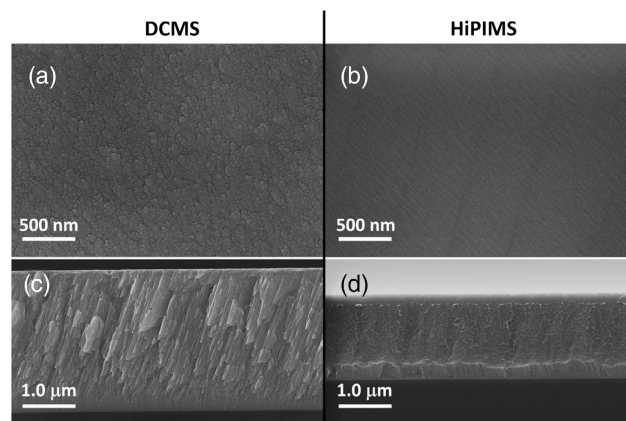


Figure 9. Secondary electron SEM images recorded from the top surfaces (a,b) and from the cross sections (c,d) of the coatings deposited by DCMS and HiPIMS.

a higher degree of self-sputtering in the former method, which reduces the amount of particles that reaches the growing film.^[83]

EDS analyses showed a homogeneous composition and a quite significant amount of oxygen in the films ($\approx 3 \text{ wt\%}$, see **Figure S8**, Supporting Information). Considering that the deposition process was performed in an inert atmosphere, the oxygen certainly comes from the sputtering target. Further work is needed in order to understand the nature of the oxide species that evidently are present in the film and the consequence of their presence on functional properties.

4. Conclusions

The academic interest in thin films of MPEAs deposited by sputtering techniques is steadily increasing. Multitarget setups are technically challenging wherefore single sputtering sources are preferred. However, currently used methods for the preparation of single multicomponent targets are rather complex and require sophisticated equipment. Hence, this work was aimed at developing a simple in-house manufacturing route of multiprincipal element sputtering sources. The chosen method consisted in pressureless sintering of cold-pressed elemental powders and was evaluated for equimolar FeNiCrCo and FeNiCrMn alloys as well as for FeNiCrCoAl_{0.4}.

XRPD data showed that the sintered pellets were composed of randomly oriented crystallites with fcc symmetry together with minor oxide phases. SEM analyses confirmed a relatively good chemical homogeneity of the MPEAs and showed that the oxides were mainly present as microsized aggregates concentrated in the porous structure of the sintered compacts. The oxide contamination was explained by passivating oxide layers already present in the starting powders that during sintering reorganized through redox reactions. The RD of the sintered pellets were high (80-90%) but not as high as those generally obtained from powder metallurgy routes employing combined compaction-sintering processes (e.g., hot isostatic pressing, spark plasma sintering). However, stable magnetron sputtering was achieved using an alloy target synthesized by the developed route. Hence,

the lower RD could be considered an acceptable trade-off for less sophisticated equipment.

Given the presence of oxygen in the target, SEM-EDS analyses showed how oxygen is also detected in deposited films. Oxygen contamination of sintered compacts is a potential drawback of powder metallurgy processing in general and methods for mitigating this problem should be evaluated, for example, by reduction of oxides in the powders followed by strict handling in inert atmosphere. Nevertheless, the nature of the oxide species in the sputtered films as well as their effect on functional properties needs further evaluation in order to determine the severity of oxide contaminants.

Supporting Information

Supporting Information is available from the Wiley Online Library or from the author.

Acknowledgements

The present work was carried out by an agreement between the Italian Ministry of Economic Development (MISE) and the National Research Council (CNR) in the framework of a Research Program for the Electric System (RdS-PAR2020). M. Zapparoli (Centro Interdipartimentale Grandi Strumenti, University of Modena and Reggio Emilia, Italy) is kindly acknowledged for technical support during FESEM analyses.

Open Access Funding provided by Università degli Studi di Modena e Reggio Emilia within the CRUI-CARE Agreement.

Conflict of Interest

The authors declare no conflict of interest.

Data Availability Statement

The data that support the findings of this study are available from the corresponding author upon reasonable request.

Keywords

high-entropy alloys, microstructures, multiprincipal element alloys, powder metallurgy, sputtering, targets

Received: November 4, 2021

Revised: January 15, 2022

Published online: March 27, 2022

- [1] B. Cantor, I. T. H. Chang, P. Knight, A. J. B. Vincent, *Mater. Sci. Eng.*, **A** **2004**, 375–377, 213.
- [2] J.-W. Yeh, S.-K. Chen, S.-J. Lin, J.-Y. Gan, T.-S. Chin, T.-T. Shun, C.-H. Tsau, S.-Y. Chang, *Adv. Eng. Mater.* **2004**, 6, 299.
- [3] Y. F. Ye, Q. Wang, J. Lu, C. T. Liu, Y. Yang, *Mater. Today* **2016**, 19, 349.
- [4] D. B. Miracle, O. N. Senkov, *Acta Mater.* **2017**, 122, 448.
- [5] E. P. George, D. Raabes, R. O. Ritchie, *Nat. Rev. Mater.* **2019**, 4, 515.
- [6] C. C. Koch, *J. Mater. Res.* **2017**, 32, 3435.
- [7] J. M. Torralba, P. Alvarado, A. García-Junceda, *Powder Metall.* **2019**, 62, 84.

- [8] M. Wang, G. Zhank, H. Cui, Y. Lu, Y. Zhao, N. Wei, T. Li, *J. Mater. Sci.* **2021**, 56, 1.
- [9] F. Yuhu, Z. Yunpeng, G. Hongyan, S. Huimin, H. Li, *Rare Metal Mat. Eng.* **2013**, 42, 1127.
- [10] K. Górecki, J. Zýka, J. Malek, J. Horvát, J. Čapek, P. Bała, *Mater. Sci. Eng.* **2017**, 179, 012027.
- [11] J. Cieslak, J. Tobola, J. Przewoznik, K. Berent, U. Dahlborg, J. Cornide, S. Mehraban, N. Lavery, M. Calvo-Dahlborg, *J. Alloys Compd.* **2019**, 801, 511.
- [12] J. Cieslak, J. Tobola, K. Berent, M. Marciszko, *J. Alloys Compd.* **2018**, 740, 264.
- [13] A. Zhang, J. Han, J. Meng, B. Su, P. Li, *Mater. Lett.* **2016**, 181, 82.
- [14] O. A. Waseem, H. J. Ryu, *Sci. Rep.* **2017**, 7, 1926.
- [15] A. Fourmont, S. L. Gallet, K. Hoummada, M. Descoins, C. Desgranges, O. Politano, F. Baras, *Mater. Chem. Phys.* **2021**, 272, 125000.
- [16] P. Veronesi, R. Rosa, E. Colombini, C. Leonelli, *Technologies* **2015**, 3, 182.
- [17] P. Veronesi, E. Colombini, R. Rosa, C. Leonelli, M. Garuti, *Chem. Eng. Process.* **2017**, 122, 397.
- [18] W. Li, P. Liu, P. K. Liaw, *Mater. Res. Lett.* **2018**, 6, 199.
- [19] X. Hui Yan, Y. Zhang, in *High Entropy Alloys, Innovations, Advances, and Applications*, (Eds.: T. S. Srivatsan, M. Gupta), CRC Press, Boca Raton, FL **2020**.
- [20] F. Mwema, E. Akinlabi, O. Oladijo, A. Baruwa, *Mater. Perform. Charact.* **2020**, 9, 528.
- [21] W. Li, P. Liu, P. K. Liaw, *Mater. Res. Lett.* **2018**, 6, 199.
- [22] V. Braic, A. Vladescu, M. Balaceanu, C. R. Luculescu, M. Braic, *Surf. Coat. Technol.* **2012**, 211, 117.
- [23] V. Dolique, A.-L. Thomann, P. Brault, Y. Tessier, P. Gillon, *Surf. Coat. Technol.* **2010**, 204, 1989.
- [24] S. K. Bachani, C.-J. Wang, P.-S. Lou, L.-C. Chang, J.-W. Lee, *Surf. Coat. Technol.* **2020**, 403, 126351.
- [25] R. Chen, Z. Cai, J. Pu, Z. Lu, S. Chen, S. Zheng, C. Zeng, *J. Alloys Compd.* **2020**, 827, 153836.
- [26] K. Fieandt, E.-M. Paschalidou, A. Srinath, P. Soucek, L. Riekehr, L. Nyholm, E. Lewis, *Thin Solid Films* **2020**, 693, 137685.
- [27] T.-H. Huang, C.-H. Hsueh, *Intermetallics* **2021**, 135, 107236.
- [28] T.-K. Chen, M.-S. Wong, T.-T. Shun, J.-W. Yeh, *Surf. Coat. Technol.* **2005**, 200, 1361.
- [29] C.-H. Lai, S.-J. Lin, J.-W. Yeh, S.-Y. Chang, *Surf. Coat. Technol.* **2006**, 201 3275.
- [30] Y.-S. Huang, L. Chen, H.-W. Lui, M.-H. Cai, J.-W. Yeh, *Mater. Sci. Eng.*, **A** **2007**, 457, 77.
- [31] M.-H. Tsai, J.-W. Yeh, J.-Y. Gan, *Thin Solid Films* **2008**, 516, 5527.
- [32] Z.-C. Chang, S.-C. Liang, S. Han, Y.-K. Chen, F.-S. Shieu, *Nucl. Instrum. Methods Phys. Res. B* **2010**, 268, 2504.
- [33] Z. F. Wu, X. D. Wang, Q. P. Cao, G. H. Zhao, J. X. Li, D. X. Zhang, J.-J. Zhu, J. Z. Jiang, *J. Alloys Compd.* **2014**, 609, 137.
- [34] Z. An, H. Jia, Y. Wu, P. D. Rack, A. D. Patchen, Y. Liu, Y. Ren, N. Li, P. K. Liaw, *Mater. Res. Lett.* **2015**, 3, 203.
- [35] Y. Ma, Y. H. Feng, Tekalign T. Debela, G. J. Peng, T. H. Zhanga, *Int. J. Refract. Hard Met.* **2016**, 54, 395.
- [36] W. Liao, S. Lan, L. Gao, H. Zhang, S. Xu, J. Song, *Thin Solid Films* **2017**, 638, 383.
- [37] T. H. Hsieh, C. H. Hsu, C. Y. Wu, J. Y. Kao, C. Y. Hsu, *Curr. Appl. Phys.* **2018**, 18, 512.
- [38] A. Nishimoto, T. Fukube, T. Maruyama, *Surf. Coat. Technol.* **2019**, 376, 52.
- [39] N. A. Khan, B. Akhavan, C. Zhou, H. Zhou, L. Chang, Y. Wang, Y. Liu, M. M. Bilek, Z. Liu, *Surf. Coat. Technol.* **2020**, 402, 126327.
- [40] N. Chawake, J. Zálešák, C. Gammer, R. Franz, M. J. Cordill, *Scr. Mater.* **2020**, 177, 22.

- [41] Y. Shi, B. Yang, P. D. Rack, S. Guo, P. K. Liaw, Y. Zhao, *Mater. Des.* **2020**, *195*, 109018.
- [42] B. Ren, Z. Shen, Z. Liu, *J. Alloys Compd.* **2013**, *560*, 171.
- [43] W. Sheng, X. Yang, C. Wang, Y. Zhang, *Entropy* **2016**, *18*, 226.
- [44] Y. S. Kim, H. J. Park, K. S. Lim, S. H. Hong, K. B. Kim, *Coatings* **2020**, *10*, 10.
- [45] A. Xia, A. Togni, S. Hirn, G. Bolelli, L. Lusvardi, R. Franz, *Surf. Coat. Technol.* **2020**, *385*, 125356.
- [46] B. R. Braeckman, D. Depla, *J. Alloys Compd.* **2015**, *646*, 810.
- [47] B. R. Braeckman, F. Boydens, H. Hidalgo, P. Dutheil, M. Jullien, A.-L. Thomann, D. Depla, *Thin Solid Films* **2015**, *580*, 71.
- [48] H. Zhang, J. Poole, R. Eller, M. Keefe, *J. Vac. Sci. Technol. A* **1999**, *17*, 1904.
- [49] T. Zuo, M. C. Gao, L. Ouyang, X. Yang, Y. Cheng, R. Feng, S. Chen, P. K. Liaw, J. A. Hawk, Y. Zhang, *Acta Mater.* **2017**, *130*, 10.
- [50] S.-M. Na, J.-H. Yoo, P. K. Lambert, N. J. Jones, *AIP Adv.* **2018**, *8*, 056412.
- [51] V. Kouznetsov, K. Macák, J. M. Schneider, U. Helmersson, I. Petrov, *Surf. Coat. Technol.* **1999**, *122*, 290.
- [52] NIST, *NIST Standard Reference Material 660a, Certificate of analysis*, National Institute of Standards and Technology (NIST), Gaithersburg, MD **2000**, NIST 660a.
- [53] A. C. Larson, R. B. Von Dreele, in *Los Alamos National Laboratory Report*, LAUR 86-748, **1994**.
- [54] B. H. Toby, *J. Appl. Crystallogr.* **2001**, *34*, 210.
- [55] T. J. Collins, *Bio Techniques* **2007**, *43*, 25.
- [56] V. Kruzhanov, *Powder Metall. Met. Ceram.* **2018**, *57*, 431.
- [57] E. Crossin, J.-Y. Yao, G. B. Schaffer, *Powder Metall.* **2007**, *50*, 354.
- [58] G. B. Schaffer, T. B. Sercombe, R. N. Lumely, *Mater. Chem. Phys.* **2001**, *67*, 85.
- [59] A. A. Sycheva, E. N. Voronina, T. V. Rakhimova, A. T. Rakhimov, *Appl. Surf. Sci.* **2019**, *475*, 1021.
- [60] C. Anders, E. M. Bringa, H. M. Urbassek, *Nucl. Instrum. Methods Phys. Res. B* **2015**, *342*, 234.
- [61] M. Fedorov, J. S. Wróbel, A. Fernández-Caballero, K. J. Kurzydłowski, D. Nguyen-Manh, *Phys. Rev. B* **2020**, *101*, 174416.
- [62] S. Lucchesi, U. Russo, A. Della Giusta, *Eur. J. Mineral.* **1997**, *9*, 31.
- [63] D. Lenaz, H. Skogby, F. Princivalle, U. Halenius, *Phys. Chem. Miner.* **2004**, *31*, 633.
- [64] J. Yang, *Acta Crystallogr. B* **2008**, *64*, 281.
- [65] W.-R. Wang, W.-L. Wang, S.-C. Wang, Y.-C. Tsai, C.-H. Lai, J.-W. Yeh, *Intermetallics* **2012**, *26*, 44.
- [66] G. Bracq, M. Laurent-Brocq, L. Perrière, *Acta Mater.* **2017**, *128*, 327.
- [67] Z. Wu, H. Bei, F. Otto, G. M. Pharr, E. P. George, *Intermetallics* **2014**, *46*, 131.
- [68] U. Dahborg, J. Cornide, M. Calvo-Dahlborg, T. C. Hansen, A. Fitsch, Z. Leong, S. Chambreland, R. Goodall, *J. Alloys Compd.* **2016**, *681*, 330.
- [69] A. Leineweber, E. J. Mittemeijer, *J. Appl. Crystallogr.* **2004**, *37*, 123.
- [70] E. J. Mittemeijer, A. B. P. Vogels, P. J. Van Der Schaaf, *J. Mater. Sci.* **1980**, *15*, 3129.
- [71] P. Scardi, M. Leoni, R. Delhez, *J. Appl. Crystallogr.* **2004**, *37*, 381.
- [72] N. A. Raftery, R. Vogel, *J. Appl. Crystallogr.* **2004**, *37*, 357.
- [73] T. Wang, L.-Q. Chen, Z.-K. Liu, *Metall. Mater. Trans.* **2007**, *38A*, 562.
- [74] F. Zhang, Y. Tong, K. Jin, H. Bei, W. J. Weber, Y. Zhang, *Entropy* **2018**, *20*, 900.
- [75] W. H. Liu, Z. P. Lu, J. Y. He, J. H. Luan, Z. J. Wang, B. Liu, Y. Liu, M. W. Chen, C. T. Liu, *Acta Mater.* **2016**, *116*, 332.
- [76] L. R. Owen, E. J. Pickering, H. Y. Playford, H. J. Stone, M. G. Tucker, N. G. Jones, *Acta Mater.* **2017**, *122*, 11.
- [77] F. Borgioli, *Metals* **2020**, *10*, 187.
- [78] B. K. Brink, K. Ståhl, T. L. Christiansen, J. Oddershede, G. Winther, M. A. J. Somers, *Scr. Mater.* **2017**, *131*, 59.
- [79] Y. Wu, W. H. Liu, X. L. Wang, D. Ma, A. D. Stoica, T. G. Nieh, Z. B. He, Z. P. Lu, *Appl. Phys. Lett.* **2014**, *104*, 051910.
- [80] H. Schwarz, T. Uhlig, N. Rösch, T. Lindner, F. Ganss, O. Hellwig, T. Lampke, G. Wagner, T. Seyller, *Coatings* **2021**, *11*, 468.
- [81] W. Li, P. Liu, P. K. Liaw, *Mater. Res. Lett.* **2018**, *6*, 199.
- [82] Y. F. Ye, Q. Wang, Y. L. Zhao, Q. F. He, J. Lu, Y. Yang, *J. Alloys Compd.* **2015**, *681*, 167.
- [83] D. Lundin, T. Minea, J. T. Gudmundsson, *High Power Impulse Magnetron Sputtering Fundamentals, Technologies, Challenges and Applications*, Elsevier, Amsterdam, The Netherlands **2019**.